CERN SUMMER STUDENT PROGRAMME REPORT

Study of the noise properties of non-destructive single-particle detector for antiproton spin flip identification

Baryon Antibaryon Symmetry Experiment - BASE

Halil Furkan KIMKAK

Supervised by

Professor Dr. Stefen Ulmer

&

Dr. Barbara Maria Latacz

Summer 2023, Geneva

Contents

Abstract

This research centres on the generation of simulation data under varied experimental parameters to predict real experimental outcomes, with a specific focus on the axial frequency in charged particle movements within magnetic traps, a critical component in understanding potential disparities between matter and antimatter. By comparing both real and simulated data, we gain an enriched perspective that bolsters our confidence in our findings, thereby guiding future experimental designs. Our approach shows a comparison between simulation and experimental data to simulate signal behaviour under diverse conditions, such as temperature fluctuations and different signal-to-noise ratios. Key to our method is the axial frequency measurement, wherein signals pass through a series of amplifiers and electronic components, culminating in an FFT signal that is later analysed. Parameters, such as noise level, resonator frequency, and the Lorentz force-induced axial frequency, are crucial for the correct interpretation of signal-frequency data. Through both experimental and simulation data analysis, the density distributions of residuals are examined, showing agreement between simulation results and real-world measurements. Additionally, using the curve fitting function from Python scipy.optimize library, we model and optimize these parameters. Our results highlight the alignment between simulated and real-world measurements, emphasizing the growing importance and accuracy of simulations in current scientific endeavours.

1. Introduction

a. BASE: Baryon Antibaryon Symmetry Experiment

The formation of the Universe, the balance of matter and anti-matter, the interactions between these phenomena, and understanding the nature of these interactions is a central topic of science, in fundamental physics. Right after the Big Bang, our universe produced equal amounts of matter and anti-matter particles.

However, the current dominance of matter in our universe and the near absence of anti-matter provide a reason for us to investigate the cause of this imbalance. In this context, the Baryon Antibaryon Symmetry Experiment (BASE) conducted at CERN is an attempt towards finding an answer to this question. The experiment aims to determine if there is any difference between the two types of particles by comparing the fundamental properties of the proton and antiproton. The Penning trap method is used in this experiment. The BASE collaboration has contributed to direct tests of CPT symmetry principle by measuring the g-factors of protons and antiprotons with unprecedented precision, at the p.p.b. level and below [1-4]. Additionally, it has compared the charge-to-mass ratios of the antiproton and proton with unparalleled precision at the $16*10^{-12}$ level [5]. BASE has improved the precision of the antiproton's magnetic moment measurement by a factor of 3000 compared to the results of competing collaborations [6]. While no evidence of CPT violation has been found in these experiments, they have presented CPT symmetry tests improved by millions of times. If a discrepancy that violates this symmetry between the proton and antiproton is found, it could lead to significant changes in the theories of physics [2].

In summary, the BASE experiment is contributing to trying to understand how matter and anti-matter were formed, how they interact, and the implications of these interactions. This experiment could yield potential results that may deepen our understanding of how came into its current existence.

b. Penning Trap

Penning traps are renowned for their ability to precisely hold charged particles for extended periods. The Earnshaw theorem states that charged particles cannot be stably stored in purely static electric or magnetic fields [7]. However, the combination of electric and magnetic fields allows for the stable containment of charged particles. In 1949, Pierce described an electron trap that has a homogeneous magnetic field in the axial direction and superimposed with a quadrupole electrostatic potential [8]. Such a structure is known as the Penning trap and is central to our experiments.

In a Penning trap, the Lorentz force acting on a charged particle compels it to move in a circular path perpendicular to the magnetic field lines. This results in what is termed the "free cyclotron frequency," denoting the periodic cyclotron motion

$$\omega_c = \frac{q}{m} B.$$

The addition of the electrostatic quadrupole potential ensures the particle's stable containment in the axial direction. Figure 1 visualizes the path followed by a particle in a Penning trap. The oscillation amplitudes and frequencies shown in the figure are for illustrative purposes and do not represent the actual values in our experiments. However, this visual is an excellent tool for understanding how a particle might move within a Penning trap.

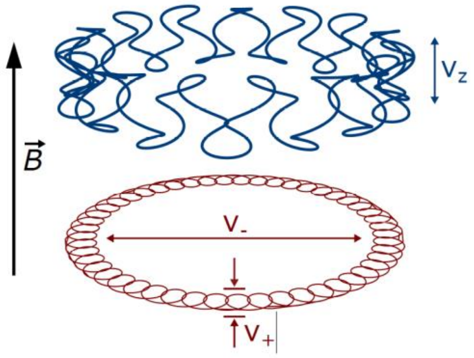

Figure 1. The fast cyclotron motion with frequency ν_+ is indicated by the small circles, while the magnetron motion within the larger circle is shown with frequency ν_-. Both motions are superimposed by the axial oscillation with frequency ν_z.

Penning traps have many advantages, but the most significant is their ability to minimize energy exchange between different motion modes. This allows particles to remain in the trap for extended periods, facilitating precise measurements [9].

c. Experimental Setup

The schematic of the BASE experiment's analysis trap setup, which consists of a cylindrical five-pole Penning trap, is shown in Figure 2 Figure 2[10]. It is positioned in the horizontal bore of a superconducting magnet. The central ring electrode, made of a cobalt-iron alloy, creates a strong magnetic inhomogeneity of approximately 300 kT/m^2, which is necessary for spin state spectroscopy by means of the continuous Stern Gerlach effect [11].

For the detection of axial motion, a feedback-cooled superconducting image current detector [12] is integrated with one of the endcap electrodes. When the antiproton in the trap comes into resonance with this circuit, it achieves thermal equilibrium with the detector. This phenomenon appears as a distinct dip in the Fourier-transformed spectrum of the detector, as represented by the blue signal in Figure 2(b). The axial oscillation frequency, ω_z, is determined by fitting these spectra using the least squares method. Notably, among the device components, the Stahl electronics UM stands out as it supplies the voltage for the trap [11].

To lower the detector's temperature to approximately T_z = 5 K, active electronic feedback has been applied [13, 14]. This adjustment narrows down the dip width to about 1 Hz [3]. With the signal-to-noise ratio considered, the quality factor has been established as Q = 21300(360). The detector's effective parallel resistance was measured to be Rp = 137(4) MΩ.

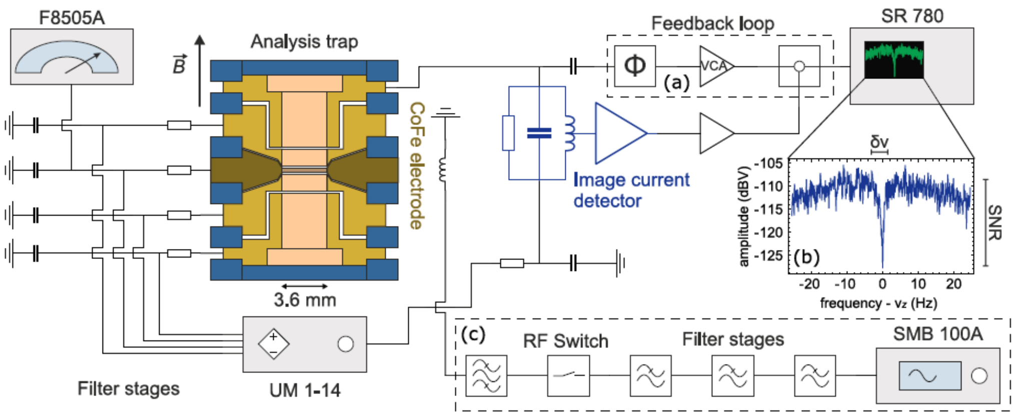

Figure 2. BASE analysis trap features gold-plated electrodes separated by sapphire spacers. The central electrode creates a magnetic field gradient. An ultra-stable voltage source powers the electrodes. Axial frequency is measured using a cooled detector (a) and signal analyser (b). A frequency generator (c) is used for particle manipulation.[11]

The entire experiment is controlled by the Control System (CS), a computer program based on the LabView 2023. (Figure 3). This control system manages devices such as high-precision voltage sources, waveform generators, and voltage sources for voltage-controllable attenuators and amplifiers [5]. This PCS runs on a PC. All DC lines in the experiment are filtered with RC circuits. The RF lines are additionally shielded with copper mesh [9].

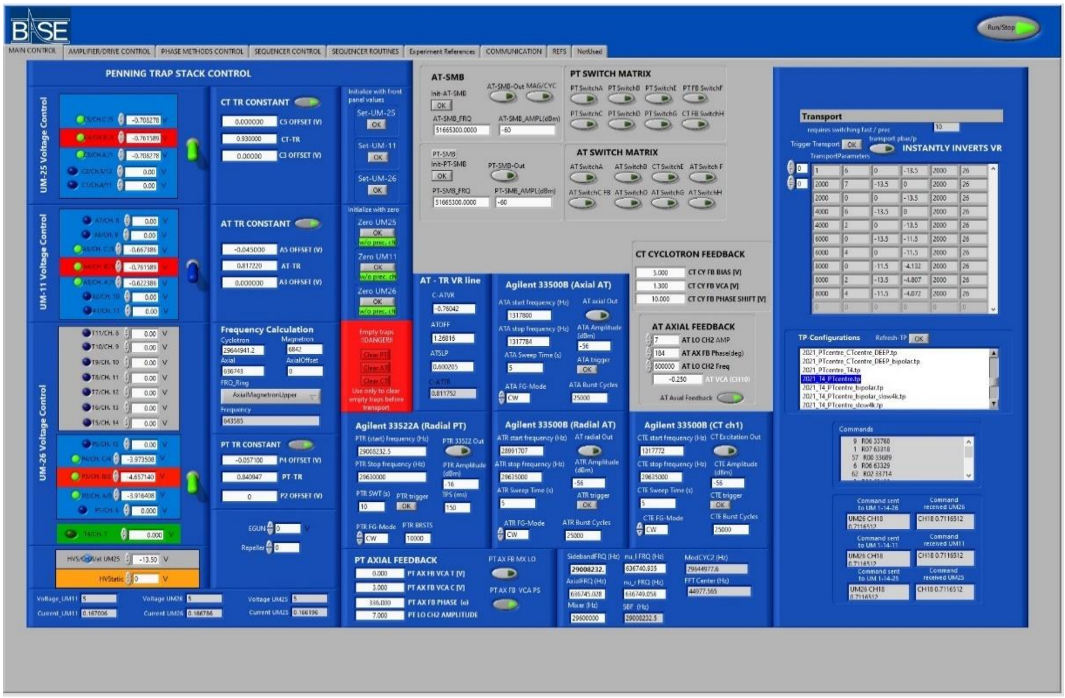

Figure 3. Capture from the Control System (CS). This virtual tool is built on LabView 2023 framework. [5]

2. Detection and Simulation Principles

Any particle stored in a Penning trap induces tiny image currents on the trap electrodes due to its motions. For the axial motion, the induced current I is related to the charge q and the velocity in the axial direction $\dot{z}$

$$I = \frac{q}{D_z}\dot{z}.$$

D_z is a geometric measure to describe how a particle couples to an electrode. For typical experimental parameters, the current is at the order of 10^{-15} A and requires a large impedance to obtain a measurable voltage signal. However, even measuring the voltage drop over an infinitely large resistance is not sufficient to obtain a significant signal. This is because of the parasitic trap capacitance C_T which is typically on the order of 10 pF. Instead of a large resistance, an inductor L_{res} is connected to the trap. The inductor and the trap capacitance form a resonance circuit described by the resonance frequency ω_{res}. C_{res} describes the inherent capacitance of the connected inductor and cannot be neglected in a real setup. The total impedance of this parallel resonance circuit is defined as $Z_{res}(\omega)$ and R_{res} is a loss component accounting for the losses in the circuit. At the resonance frequency w_{res}, the capacitive component is compensated by the inductance and the total impedance becomes R_{res}. Therefore, a resonator with a sufficiently high parallel resistance is suitable to detect the tiny image currents and achieve a measurable voltage drop. To compute the line shape of the dip spectrum, a lumped circuit model is used. In this model, the particle is modelled as a series-tuned RLC circuit, while the resonator is modelled as a parallel-tuned RLC circuit (**Figure 4**) [15].

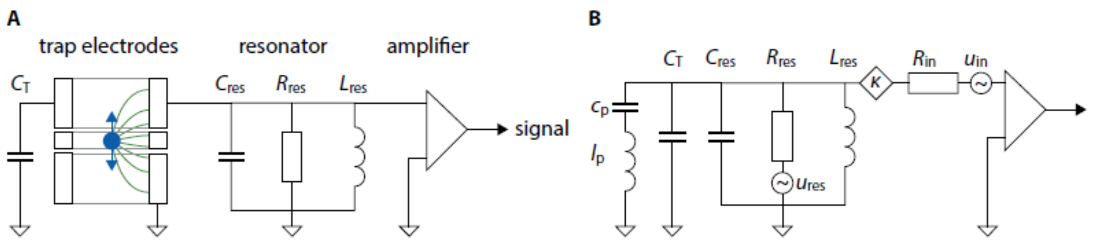

Figure 4. Part A: In the Penning trap, the particle causes minor image currents on the electrodes. These currents are detected via a tuned resonant circuit, amplified, and analysed with Fast Fourier Transformation to measure the proton's motions. Part B: The particle's equivalent circuit diagram showcases a series resonance circuit with two noise sources for the resonator's Johnson-Nyquist noise and the amplifier's input resistance noise. The term 'k' indicates the amplifier's decoupling from the resonator, typical in experiments [15].

In the equation, $Z(w)$, the parallel impedance of the particle and resonator is specified

$$Z(w) = \left(\frac{1}{iwc_1 + iwl_1 + r_1} + iwC_0 + \frac{1}{iwL_0} + \frac{1}{R_0}\right)^{-1}.$$

The variables in these equations represent the components of the electric circuit (resistance, inductance, and capacitance). For simplification, C_0 and c_1 are defined here

$$C_0 = \frac{1}{w_0^2 L_0}, \qquad c_1 = \frac{1}{w_1^2 l_1} \ .$$

The Johnson-Nyquist noise is defined in the equation u_n. This noise is known as the random fluctuations caused by an electric current flowing over any resistance. Here, the real part of the impedance is taken as the resistance component.

$$u_n = \sqrt{4k_B T D_n \text{Re}[Z]} \ .$$

The real part of the impedance, i.e., Re$[Z]$, is expressed by terms A, B, C, and D. These terms describe the frequency-dependent behaviors of the components of the circuit

$$\text{Re}[Z] = \frac{A}{B + C + D}$$

$$A = L_0^2 R_0 w^2 w_0^4 (R_0 r_1 w^2 + r_1^2 w^2 + l_1^2 (w^2 - w_1^2)^2)$$

$$B = 2L_0^2 R_0 r_1 w^4 w_0^4$$

$$C = L_0^2 w^2 w_0^4 (r_1^2 w^2 + l_1^2 (w^2 - w_1^2)^2)$$

$$D = R_0^2 \left(r_1^2 (w^3 - w w_0^2)^2 + \left(L_0 w^2 w_0^2 - l_1 (w^2 - w_0^2)(w^2 - w_1^2) \right)^2 \right).$$

Combining these formulas with the Johnson-Nyquist noise equation yields $u_{\log}$ expressed in a logarithmic scale

$$u_{\log} = 20 \log\left(\sqrt{4 k_B T D_n \mathrm{Re}[Z]}\right).$$

The definition of the single dip is based on a simplified line shape model given by the equation $r(\nu)$. This model describes a spectrum as a function of frequency. With this equation, we can obtain a line shape that fits a real dip spectrum [15]

$$r(\nu) = n_0 + \frac{4(\nu - \nu_1)^2 n_1}{d_1^2 \left(\frac{4(\nu - \nu_1)^2}{d_1^2} + \left(1 - \frac{4(\nu - \nu_0)(\nu - \nu_1)}{d_0 d_1} \right)^2 \right)}.$$

In this model, n_0 and n_1 define the offset in the spectrum (i.e., the initial value) and the signal-to-noise ratio respectively. The width and frequency of the dip are controlled by d_1 and ν_0 while for the resonator it occurs with d_0 and ν_0.

In the basic model, the "dip" always shorts the resonator perfectly. This means that the background of the resonator, the n_0 value, is at the same level as the minimum value of the dip [15].

a. Gaussian and Rayleigh Distributions

Gaussian distribution is commonly encountered in random processes, physical events, and engineering applications. In resonance circuits, the intensity or phase of the signal may vary with a Gaussian distribution. Particularly, the complex Gaussian distribution is utilized to model how the amplitude or phase of a signal changes over time in a resonance circuit. In this distribution, the real and imaginary components of a random variable are independent and identically distributed. This is crucial when analysing the spectral components of the signal. This distribution, also known as the bell curve, is defined by the probability density function (pdf) of random variables:

$$f(x|\mu, \sigma^2) = \frac{1}{\sigma\sqrt{2\pi}} e^{-\frac{(x-\mu)^2}{2\sigma^2}}.$$

In this formula, μ represents the mean, and σ the standard deviation. In this study, during the simulation of the signal in the resonance circuit, it is used to produce Gaussian-distributed random numbers for the signal's spectral components.

Rayleigh distribution is used particularly in the wireless communication field to model the distribution of signal amplitude. It is defined as the distribution of the square root of the sum of squares of two independent random variables, each having a standard normal (Gaussian) distribution. Specifically, if X and Y are independent random variables with a standard normal distribution (mean 0 and equal variances), then the random variable Z is:

$$Z = \sqrt{X^2 + Y^2}.$$

This means that the random variable *Z* follows the Rayleigh distribution. The probability density function (pdf) of the Rayleigh distribution is:

$$f(z) = \frac{z}{\sigma^2} e^{-\frac{z^2}{2\sigma^2}} \quad \text{for} \quad z \geq 0\,.$$

Here, σ is a positive scale parameter. The expected value (mean) and variance of the Rayleigh distribution are:

$$\mu = \sigma\sqrt{\frac{\pi}{2}}$$

$$\sigma_Z^2 = \frac{4-\pi}{2}\sigma^2\,.$$

When simulating the signal in a resonance circuit, the response of this circuit shows amplitude fluctuations. In this case, the Rayleigh distribution can be used to describe the distribution of these unpredictable amplitude fluctuations. According to the Johnson-Nyquist theorem, there is thermal noise directly related to the temperature of a conductor. This thermal noise causes fluctuations in the amplitude of the circuit signal. Therefore, modelling with Rayleigh distribution is necessary to simulate this noise.

b. Johnson Nyquist Noise

The Johnson-Nyquist theorem describes the noise arising in a resistor due to thermal motion. This noise can be found in every electronic circuit and can affect the signal-to-noise ratio. Especially, the spectral density of this noise changes as a function of the resistance and temperature. Particularly when working at low signal levels, this noise can seriously affect the overall performance of the circuit. It is critically important to choose the right component values to ensure that the noise level is sufficiently low. This is especially important in measurement and analysis applications because the signal-to-noise ratio is critical for measurement accuracy.

This noise was first discovered by John B. Johnson in 1928. Later, his colleague Harry Nyquist provided a theoretical explanation for these observations based on Johnson's findings. The Johnson-Nyquist theorem states that the thermal noise power in a circuit over a bandwidth is directly related to the resistance and temperature of that circuit.

The spectral density of this noise is usually denoted by $\mathrm{S(f)}$ and is defined as:

$$S(f) = 4k_BTR\,.$$

Here, $\mathrm{S(f)}$ noise density (expressed in W/Hz or V^2/Hz), $\mathrm{k_B}$ Boltzmann constant (1.38×10^{-23} J/K), T absolute temperature (in Kelvin), R resistance of the circuit (in Ohms).

The effective value (rms) of the noise signal amplitude can be found from:

$$u_n = \sqrt{4k_BTD_n\mathrm{Re}[Z]}\,.$$

Here, $\mathrm{D_n}$ bandwidth (in Hz), Re$[\mathrm{Z}]$ is real impedance of the circuit. This formula gives the effective noise voltage for a given bandwidth. As the bandwidth increases, the noise voltage also increases.

c. Allan and BASE Allan Deviations

The Allan deviation (or Allan variance) is a method used to evaluate the statistical stability of a measurement series. It is typically used to analyse variations in a frequency or time measurement series. For a given set of N data points $\mathrm{x_i}$ with a sample rate $\mathrm{f_s}$ and averaging time τ (non-overlapping), the Allan deviation is defined as:

$$\sigma_A(\tau) = \sqrt{\frac{1}{2(n-1)} \sum_{k=1}^{n-1} (\bar{x}_{k+1} - \bar{x}_k)^2} \, .$$

Where $\bar{x}_k$ is the k-th average during the observation time τ, and $n = \frac{N}{f_s \tau}$ is the size of the averages $\bar{x}_k$ sequence. For the averaging time τ equal to the sampling period $\tau = \frac{1}{f_s}$, the average series becomes:

$$\bar{x}_k = x_i$$

and the Allan deviation is:

$$\sigma_A = \sqrt{\frac{1}{2(N-1)} \sum_{i=1}^{N-1} (x_{i+1} - x_i)^2} \, .$$

In the case of white noise, this expression is very similar to the regular standard deviation and should yield similar (but not identical) results.

As for Base Allan Deviation details, for a given set of N data points x_i with a sample rate f_s and averaging time τ (non-overlapping), the Base Allan deviation is defined as:

$$\sigma_B(\tau) = \sigma(\bar{x}_{k+1} - \bar{x}_k)$$

$$\sigma_B = \sqrt{\frac{1}{n-2} \sum_{k=1}^{n-1} (\bar{x}_{k+1} - \bar{x}_k - \langle \bar{x}_{k+1} - \bar{x}_k \rangle)^2}$$

$$\sigma_B = \sqrt{\frac{1}{n-2} \sum_{k=1}^{n-1} \left(\bar{x}_{k+1} - \bar{x}_k - \frac{\bar{x}_n - \bar{x}_1}{n-1} \right)^2} .$$

Where $\bar{x}_k$ is the k-th average during the observation time τ, and $n = \frac{N}{f_s \tau}$ is the size of the averages $\bar{x}_k$ sequence. This definition differs from the equation above by the linear drift correction term in the sum of squares. For the averaging time τ equal to the sampling period $\tau = \frac{1}{f_s}$ the average series becomes:

$$\bar{x}_k = x_i$$

and the Base Allan deviation is:

$$\sigma_B = \sqrt{\frac{1}{N-2} \sum_{i=1}^{N-1} \left(x_{i+1} - x_i - \frac{x_N - x_1}{N-1} \right)^2} \, .$$

Allan deviation and Base Allan deviation are valuable tools used to understand how the variance in a measurement series evolves. Different noise types, such as white noise, flicker noise, or frequency-fixed deviations, result in distinct shapes and trends in Allan deviation plots. This is extremely useful for characterizing or optimizing a measurement system.

3. Motivation and Goals

Central to our research is the aspiration to generate simulation data under various experimental parameters, serving as preliminary knowledge for predicting real experimental outcomes. The integration of both real and simulated data provides an expansive overview, enhancing confidence in our findings and offering guidance for future experimental designs. We aim to explore, through simulations, the behaviour of signal data under various conditions - be it temperature variations, changes in average measurement duration, different resistance values, or desired different signal-to-noise ratios. Our immediate goal is to juxtapose real experimental data with our simulation outcomes, aiming to refine the simulation algorithm development through continuous comparison with real-world data. Broadly, our journey to simulate a signal is driven by a multifaceted goal as well: to validate real-world data, pinpoint anomalies, or outliers, and establish a foundation for future predictions.

4. Mission

In axial frequency measurement, after the resonance circuit goes through a set of amplifiers and electronic components, the FFT signal is obtained and examined. In a situation we want to simulate, we present some input parameters to the system, and the start of this is the line-shape. Among these parameters are the noise level of the resonator (n_0[dB]), the maximum signal level of the resonator (n_1[dB]), resonator frequency (f_0[Hz]), the width of the resonator (df_0[Hz]), the dipping frequency (f_1[Hz]), and the width of the dip (df_1[Hz]). These parameters play a critical role in interpreting the signal-frequency data obtained with the FFT analyser correctly. As stated in Section **Detection and Simulation Principles**, measuring and evaluating these parameters results in a specific line-shape formula. When used with the input parameters presented in Table 1, this formula achieves the signal-frequency line shape shown in Figure 5.

Table 1. The parameters of the fit

Parameters	Value	Unit
Resonator Noise Level (n_0)	-92.408837	dB
Resonator Maximum Signal Level (n_1)	-79.050989	dB
Resonator Frequency (f_0)	65927.078141	Hz
Width of the Resonator (f_1)	65927.266612	Hz
Particle Dip Frequency (df_0)	46.709437	Hz
Width of the Dip (df_1)	2.311618	Hz

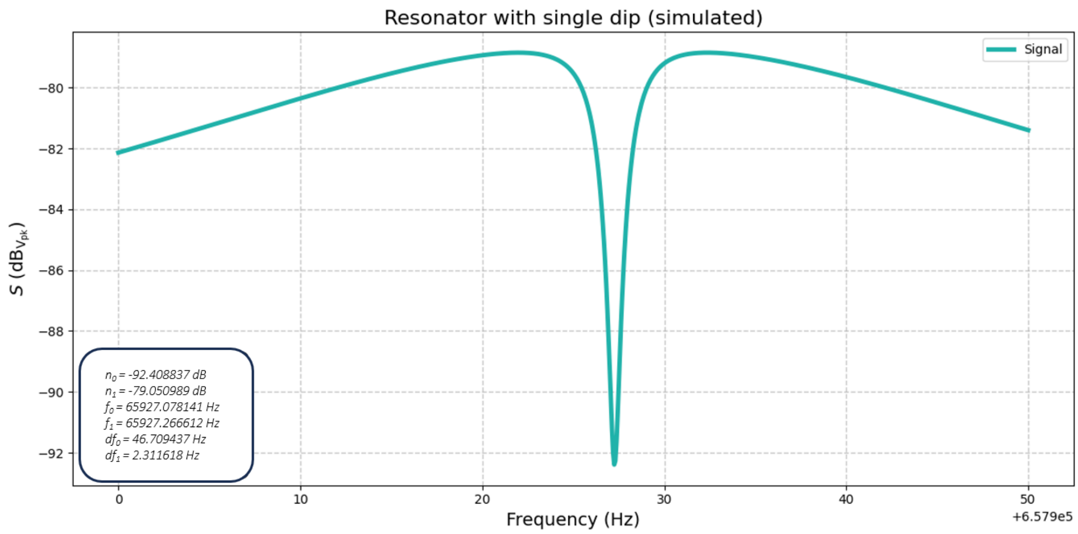

Figure 5. After applying the fit parameters to the line-shape formula, the resulting signal profile

In the Figure 6, each data point is a value that comes from a Gauss distribution determined randomly over a value range. This range is defined by the sigma value of the Gaussian distribution. The sigma value is determined according to the Johnson-Nyquist theorem discussed in detail in the **Johnson Nyquist Noise** section. The S (dB_{Vpk}) values forming the turquoise signal in Figure 5 are the Re[Z] values found in the Johnson-Nyquist noise formula. The given bandwidth value, together with temperature and Boltzmann constant, is used to calculate the value used as sigma for the Gaussian distribution. This characteristic naturally brings different density values due to the nature of the simulation. These derived sigma values have been used to produce random numbers determined using the Gaussian Distribution detailed in the **Gaussian and Rayleigh Distributions**, and these numbers are presented in Figure 6.

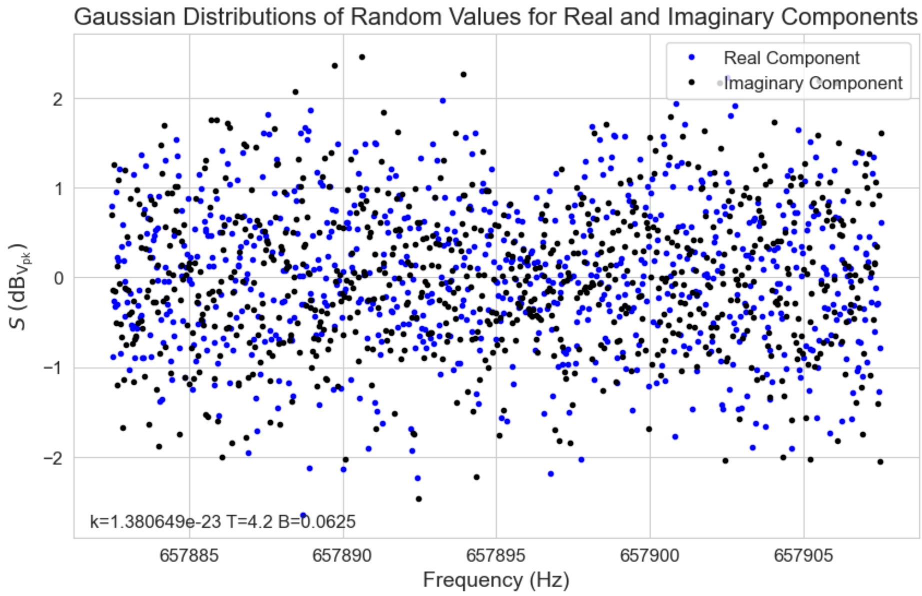

Figure 6. Gaussian distribution representation of random values for the real and imaginary components in signal processing

When we focus on the circuit components discussed in detail in the section **Detection and Simulation Principles**, the power of the complex number obtained while determining the voltage value of the equivalent circuit is calculated, and the Fourier Transform (FFT) is taken for analysis. The reason for generating random numbers for both real and imaginary parts during the Gaussian distribution formation is this. In laboratory experiments, it has been observed that the obtained data sets are measured several times and averaged; this can vary from one experiment to another. Especially when taking four 16-second measurements over 64 seconds and averaging them. Therefore, the numbers generated from the Gaussian distribution are prepared to simulate these measurement durations and averaging processes. If four different average values are taken, for each line shape point, a total of eight Gaussian numbers are produced for both real and imaginary components. For these calculations, a total of 8 random numbers are generated, accounting for both the real and imaginary parts. Each number is squared, then summed, and the result is divided by 8. Finally, the square root of this average is taken (Figure 7).

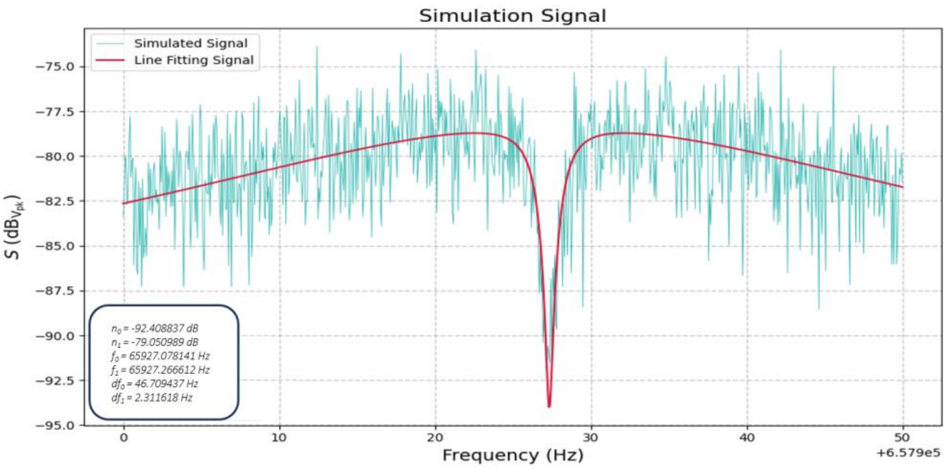

Figure 7. Comparison of the simulated signal with the line-fitted signal derived from data analysis.

For the comparison of residuals in the density histogram, the residuals of both signals shown in Figure 8 need to be identified. In the process of fitting experimental and simulation data and calculating their residuals, the curve_fit algorithm from Python's scipy.optimize library was adopted as a curve-fitting approach. This approach is applied to both experimental and simulation data. The main aim behind this approach was to derive a robust model that would closely fit the observed data. The curve_fit function was used in our method. Its primary goal is to fit a particular function to experimental data. In other words, given a certain function model and observation data, this function optimizes the parameters of this model, ensuring the model fits the data in the best possible way.

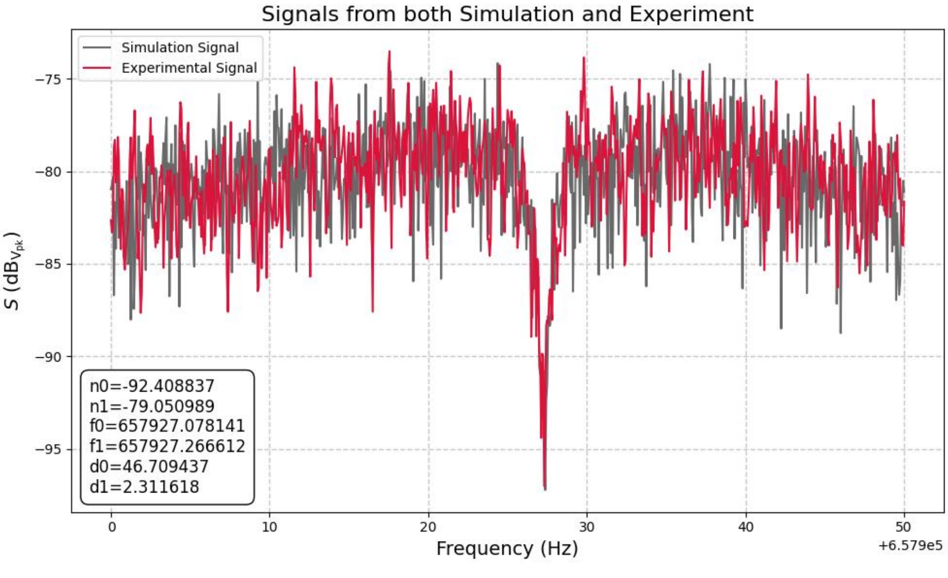

Figure 8. Depiction of signals derived from both simulation and experimental measurements for comprehensive analysis

5. Result

In our study, we focused on how the residual values related to a selected measurement set are distributed and how this distribution correlates with simulation results.

In this analytical approach, the density distributions of histograms presented in Figure 9 detail how both the residuals from experimental data and residuals from the specially constructed simulation signal for this measurement show their distribution. The main reason behind using these density-based histograms is to normalize data sets and achieve a total area value of one. This ensures more objective and consistent results when comparing data sets with different sample sizes. This process assists us in validating the integrity and representativeness of data sets and also highlights the alignment between different simulations and real-world measurements.

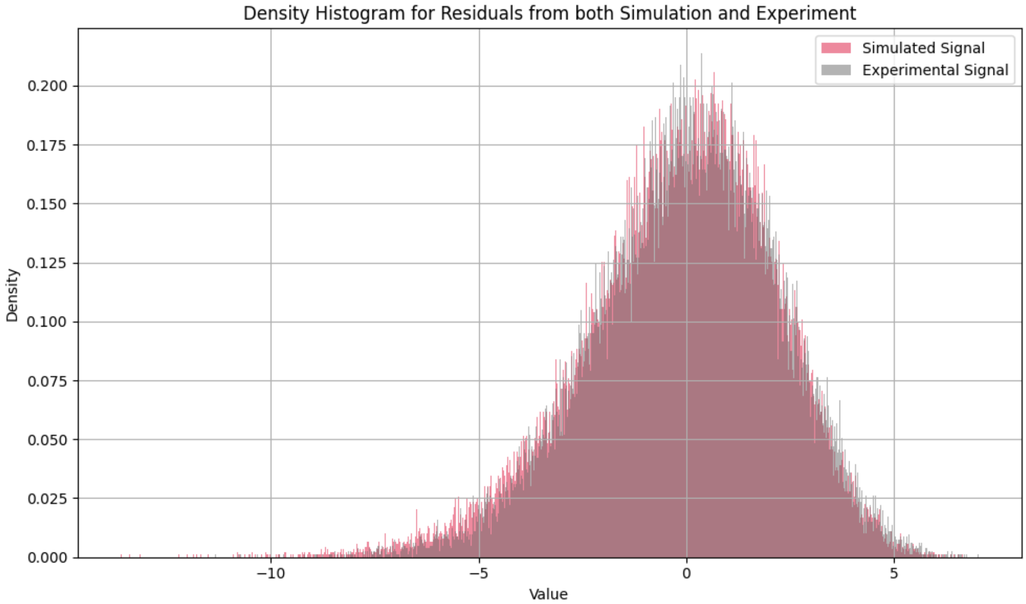

Figure 9. Histogram showcasing the density distribution of residuals obtained from both simulation and experimental data.

6. Conclusion

In conclusion, obtaining noisy signals via simulation, especially in complex systems, is of vital importance for ensuring a correct representation. Checking the accuracy of such signals is a critical process in terms of the reliability of the research and the validity of the results. In this verification process, the BADEV (Base Allan Deviation) provides very useful metrics to compare and evaluate different data sets. Comparing experimental data with simulation results, we can see that these two data sets have similar trends and characteristics. This becomes more evident in the right graph of **Figure 10**, which displays BADEV values obtained from the experimental data set, while the left graph of **Figure 10** visualizes the analysis results of the simulation data set. The remarkable consistency between these two charts indicates how successfully and accurately our simulation algorithm can mimic real-world data. This emphasizes the significance of such algorithms in an era where the role of simulation and modelling is increasing in modern research.

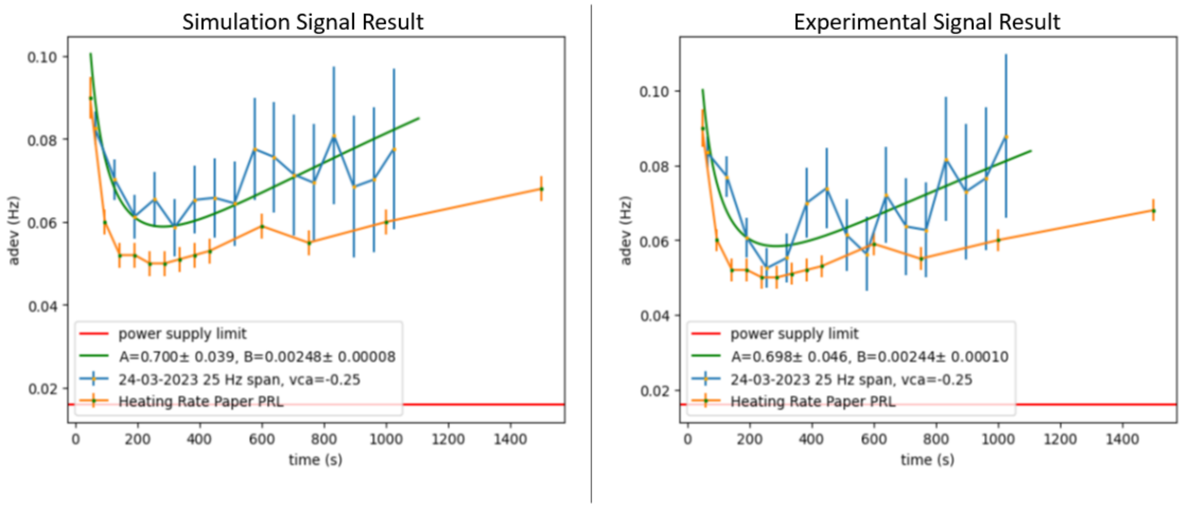

Figure 10. On the left side, results obtained from simulations are presented. The graph on the right displays experimental outcomes representing the actual results. The horizontal red line depicted in the graphs represents the power supply limit. This line is anchored at a value of 0.016 on the y-axis. The blue line delineates the badev (Base Allan Deviation) values measured at specific temporal intervals. The measurement uncertainty associated with the badev values is also indicated on this line with orange-coloured error bars. As discerned from the label, this dataset was procured on March 24, 2023, with a span of 25 Hz, and additional details regarding the span and vca value from which these values were ascertained are also provided. The green line portrays the fitted data curve. The orange line, conversely, represents data corresponding to the heating rate.

7. Outlook

While the current scope of our research has provided substantial groundwork, there remains uncharted territory we had aspired to delve into. Specifically, the anticipation is to utilize the developed methodologies to study the ADEV based on simulation, taking into account variables such as time, dip width, and the signal-to-noise ratio. The tools and techniques we have refined in the course of our work pave the way for future endeavours in this direction. It's our optimistic view that the foundational developments we've achieved will be instrumental in furthering research, providing a roadmap for subsequent studies aiming to harness the potential of these simulations for advanced experimental predictions.

8. References

1. Schneider, G., et al., *Double-trap measurement of the proton magnetic moment at 0.3 parts per billion precision.* Science, 2017. **358**(6366): p. 1081-1084.
2. Smorra, C., et al., *BASE–the baryon antibaryon symmetry experiment.* The European Physical Journal Special Topics, 2015. **224**: p. 3055-3108.
3. Nagahama, H., et al., *Sixfold improved single particle measurement of the magnetic moment of the antiproton.* Nature communications, 2017. **8**(1): p. 14084.
4. Mooser, A., et al., *Direct high-precision measurement of the magnetic moment of the proton.* Nature, 2014. **509**(7502): p. 596-599.
5. Ulmer, S., et al., *High-precision comparison of the antiproton-to-proton charge-to-mass ratio.* Nature, 2015. **524**(7564): p. 196-199.
6. DiSciacca, J., et al., *One-particle measurement of the antiproton magnetic moment.* Physical review letters, 2013. **110**(13): p. 130801.
7. Earnshaw, S., *On the nature of the molecular forces which regulate the constitution of the luminiferous ether.* Transactions of the Cambridge Philosophical Society, 1848. **7**: p. 97.
8. Pierce, J., *Theory and Design of Electron Beams, D. Von Nostrand Co.* Inc. New york, 1940.
9. Ulmer, S., *First observation of spin flips with a single proton stored in a cryogenic Penning trap*. 2011, Ruprecht-Karls-Universität Heidelberg, Germany.
10. Gabrielse, G., L. Haarsma, and S. Rolston, *Open-endcap Penning traps for high precision experiments.* International Journal of Mass Spectrometry and Ion Processes, 1989. **88**(2-3): p. 319-332.
11. Borchert, M.J., *Challenging the Standard Model by high precision comparisons of the fundamental properties of antiprotons and protons.* 2021.
12. Wineland, D. and H. Dehmelt, *Principles of the stored ion calorimeter.* Journal of Applied Physics, 1975. **46**(2): p. 919-930.
13. Dehmelt, H., W. Nagourney, and J. Sandberg, *Self-excited mono-ion oscillator.* Proceedings of the National Academy of Sciences, 1986. **83**(16): p. 5761-5763.
14. d'Urso, B., B. Odom, and G. Gabrielse, *Feedback cooling of a one-electron oscillator.* Physical review letters, 2003. **90**(4): p. 043001.
15. Schneider, G., *300 ppt Measurement of the Proton g-Factor*. 2017, Dissertation, Mainz, Johannes Gutenberg-Universität, 2018.